Dual Excited-State Intramolecular Proton Transfer Reaction in 3-Hydroxy-2-(pyridin-2-yl)-4*H*-chromen-4-one

Chyi-Lin Chen,[†] Chun-Wei Lin,[†] Cheng-Chih Hsieh,[†] Chin-Hung Lai,[†] Gene-Hsiang Lee,[‡] Chih-Chieh Wang,[§] and Pi-Tai Chou*,[†]

Department of Chemistry, National Taiwan University, Taipei, 106, Taiwan, R.O.C., Instrumentation Center, National Taiwan University, Taipei, Taiwan, R.O.C., and Department of Chemistry, Soochow University, Taipei, Taiwan, R.O.C.

The synthesis, characterization and fundamental of the dual excited-state proton-transfer properties of 3-hydroxy-2-(pyridin-2-yl)-4*H*-chromen-4-one (**1a**) are reported. In the electronic ground state, there exist two competitive hydrogen bonding (HB) isomers for **1a**. Conformer **1a(O)** reveals a five-membered ring HB structure between O−H and carbonyl oxygen, while conformer **1a(N)** possesses a six-membered ring HB formation between O−H and pyridyl nitrogen. In a single crystal, the X-ray crystallography unveils an exclusive formation of conformer **1a(N)**. In solution such as CH$_2$Cl$_2$, **1a(O)** and **1a(N)** are in equilibrium, and their respective absorption chromophores are significantly different due to different degrees of hydrogen-bond induced π electron delocalization. Upon excitation, both conformers **1a(O)** and **1a(N)** undergo excited-state intramolecular proton transfer (ESIPT) reaction. Following ESIPT, **1a(O)** gives rise to a tautomer emission maximized at 534 nm in CH$_2$Cl$_2$. Conversely, due to dominant radiationless quenching processes the tautomer emission for **1a(N)** cannot be obtained with a steady-state manner but can be resolved from time-resolved fluorescence. Time resolved fluorescence estimates an equilibrium constant of 27 ± 5 in favor of **1a(N)** in CH$_2$Cl$_2$. Ultrafast ESIPT also takes place for the unique **1a(N)** form in the crystal. Due to the prohibition of quenching processes in the solid state, bright tautomer emission maximized at 540 nm is resolved for **1a(N)** ($\Phi_f \sim 0.3$). The interplay between two HB conformers with on(**1a(O)**)/off(**1a(N)**) character in tautomer emission may find future applications such as the recognition of organic Lewis acid/base in organic solvents.

1. Introduction

Proton transfer has been ubiquitously found in chemical and biological reactions.[1] Among various types of proton transfer patterns, the category relevant to excited-state intramolecular proton transfer (ESIPT) has received much attention owing to the simplicity of its reaction pattern. Numerous ESIPT molecules have been strategically designed and synthesized in an aim to shed light on the fundamental in proton-transfer mechanism[2] and/or to explore their potential applications (we cite only a small selection of representative reports).[3]

In terms of hydrogen bonding (HB) structure, most ESIPT molecules possess either five- or six- membered ring hydrogen bonds between O−H (or N−H) and C=O (or pyridinic nitrogen). Recently, we have explored a new class of ESIPT molecules bearing a seven-membered ring HB structure akin to the core chromophore of the green fluorescence protein.[4] Among those ESIPT molecules possessing five-membered-ring hydrogen bond, 3-hydroxyflavone (3HF, see Scheme 1) has been considered a paradigm ever since its ESIPT property was discovered by Kasha and co-workers.[5] In nonpolar solvent such as cyclohexane, 3HF exhibits the S$_0 \rightarrow$ S$_1$ ($\pi\pi^*$) transition maximized at 340 and 354 nm, while the fluorescence of 3HF shows an anomalously large Stokes shifted band maximized at $\sim$526 nm ($\Phi = 0.36$, $\tau_f = 3$ ns).[6] Upon methylating 3HF to

form 3-methoxyflavone, 3-methoxyflavone shows normal Stokes shifted fluorescence maximized at $\sim$360 nm in cyclohexane.[6d] It is thus concluded that ESIPT takes place from the hydroxyl proton to the carbonyl oxygen, giving rise to the proton-transfer tautomer emission. Due to its relatively weak, five-membered ring hydrogen bond (c.f. six-membered ring hydrogen bond), 3HF was once adopted as a model compound to demonstrate appreciable barrier during ESIPT. Subsequently, it was found that the retardation of ESIPT at low temperature is mainly due to the external HB interaction caused by traces of protic solvent impurity (e.g., water, alcohols) present in the nonpolar solvents.[6a] In the dry, extensively purified nonpolar solvent such as cyclohexane, the time-resolved measurement rendered an ultrafast time of ESIPT for 3HF ($\tau_{pt} < 240$ fs),[6f−i] and ESIPT is essentially barrierless, which is perhaps induced by the low frequency, skeletal motions associated with the hydrogen bond.[7]
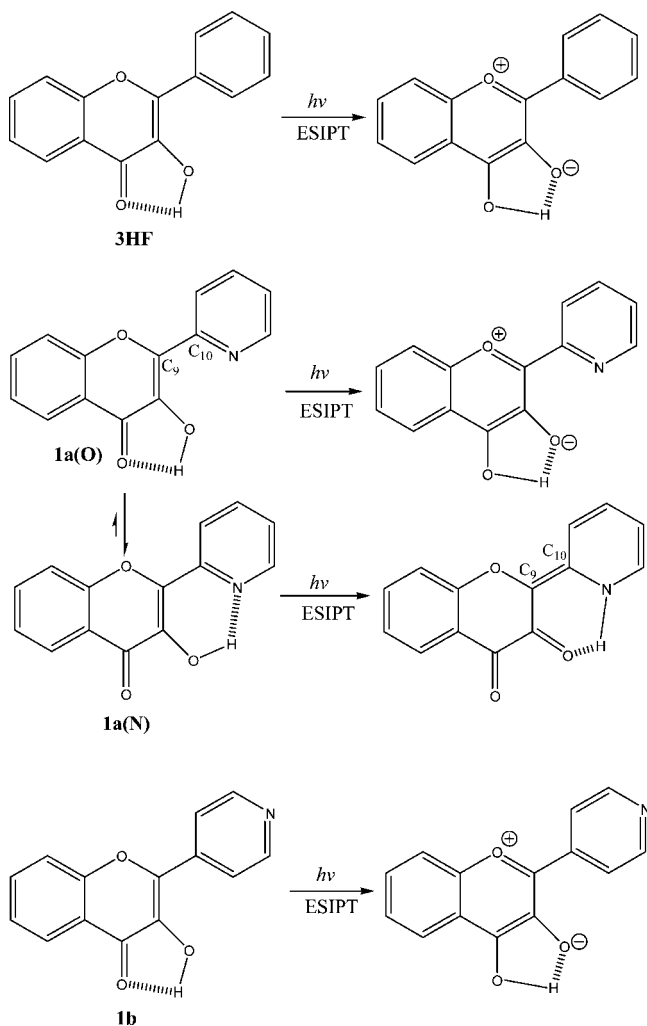
In yet another approach, study of ESIPT coupled excited-state intramolecular charge transfer (ESICT) by strategically functionalizing 3HF with electron donating substituents has been an intriguing fundamental topic. Using 4'-*N*,*N*-diethylamino-3-hydroxyflavone (see Scheme 2) as an example,[8] upon excitation, adiabatic, ultrafast charge transfer takes place from the diethyl-amino moiety to the carbonyl oxygen, resulting in a charge transfer state (CT*, * denotes the electronically excited state, see Scheme 2). After solvent relaxation, the equilibrated CT*, CT$_{eq}$*, then undergoes CT$_{eq}$* $\rightarrow$ PT$_{eq}$* (PT denotes the proton transfer tautomer) proton transfer. Due to the great difference in equilibrium polarization between CT$_{eq}$* and PT$_{eq}$* (see Scheme 2), a solvent polarity induced barrier is introduced,

* Corresponding author. Telephone: +886-2-33663894. Fax: +886-2-23695208. E-mail: chop@ntu.edu.tw.
† Department of Chemistry, National Taiwan University.
‡ Instrumentation Center, National Taiwan University.
§ Department of Chemistry, Soochow University.

206 *J. Phys. Chem. A, Vol. 113, No. 1, 2009*

Chen et al.

SCHEME 1: Molecular Structures of 3HF, 1a (Isomer Included), 1b, and Their Respective ESIPT Processes

pathways and hence the possible ratiometric emission may provide latent applications in e.g. molecular recognition. Details of the results and discussion are elaborated in the following sections.

2. Experimental Section

Scheme 3 depicts synthetic routes of **1a** and **1b**. All reactions were performed under nitrogen. Solvents were distilled from appropriate drying agents prior to use. Commercially available reagents were used without further purification unless otherwise stated. All reactions were monitored by TLC with Merck precoated glass plates (0.20 mm with fluorescent indicator UV254) and were visualized with UV light irradiation at 254/366 nm. Flash column chromatography was carried out with the use of silica gel from Merck (230−400 mesh). Mass spectra were obtained on a JEOL SX-102A instrument operating in electron impact (EI) or fast atom bombardment (FAB) mode. The ^{1}H and ^{13}C NMR spectra were obtained on Bruker spectrometers operating at frequencies as indicated for each compound. Chemical shifts were reported relative to CDCl$_3$ (^{1}H 7.24) and at 77.0 ppm in CDCl$_3$ [^{13}C (central line of t)]. FT-IR spectra were recorded on a Nicolet magna-IR 550 series II. Melting points were uncorrected.

General Procedure for the Synthesis of Chalcones. KOH (2.9 equiv) was added to a suspension of relevant aldehyde (1.0 equiv, see Scheme 3) and the appropriate acetophenone (1.05 equiv) in EtOH (6 mL/mmol acetophenone). The mixture was stirred at 50 °C for 3 h, then cooled down to room temperature and left overnight. The reaction mixture was poured into water and acidified with aqueous HCl (1 M) to obtain the corresponding chalcones (**a** or **b**) that could be further crystallized in EtOH. Spectroscopic and analytical data for **a** and **b** are shown below.

(*E*)-1-(2-Hydroxyphenyl)-3-(pyridin-2-yl)prop-2-en-1-one (a). Using picolinaldehyde (1.5 mL, 15 mmol) gave 2.6 g (76%) of **a**, which was further recrystallized from EtOH. ^{1}H NMR: δ 12.7 (s, 1H), 8.6 (d, *J* = 4.0 Hz, 1H), 8.2 (d, *J* = 15.2 Hz, 1H), 8.0−7.8 (m, 1H), 7.7 (d, *J* = 1.6 Hz, 1H), 7.84−7.48 (m, 1H), 7.47−7.44 (m, 1H), 7.30−7.28 (m, 1H), 7.27−6.98 (m, 1H), 6.94−6.90 (m, 1H). ^{13}C NMR: δ 193.8, 163.3, 152.5, 150.0, 143.0, 136.8, 136.5, 130.1, 125.7, 124.5, 123.9, 119.9, 118.8, 118.3.

(*E*)-1-(2-Hydroxyphenyl)-3-(pyridin-4-yl)prop-2-en-1-one (b). Using isonicotinaldehyde (1.5 mL, 15 mmol) gave 2.2 g (65%) of **a**, which was further recrystallized from EtOH. ^{1}H NMR: δ 7.92−7.88 (m, 2H), 7.56−7.52 (m, 1H), 7.48−7.43 (m, 2H), 7.30−7.26 (m, 1H), 7.23−7.20 (m, 1H), 6.97(d, *J* = 19, 1H), 6.91−6.87 (m, 1H). ^{13}C NMR: δ 161.8, 147.0, 135.8, 133.1, 130.6, 125.7, 123.3, 123.0, 122.9, 119.0, 117.4, 112.3.

General Procedure for the Synthesis of 3-Hydroxy-2-(pyridinyl)-4*H*-chromen-4-one. Aqueous 30% H$_2$O$_2$ (8−11 equiv) was added to a solution of the appropriate chalcone (**a** or **b**, see Scheme 3) (1.0 equiv) and aqueous 4 M NaOH (5.0 equiv) in a 1:1 mixture of MeOH and THF (20 mL/mmol chalcone) at 0 °C. The reaction was stirred at room temperature overnight. The mixture was then acidified with aqueous HCl (1 M) and the product filtered off. Spectroscopic and analytical data for **1a** and **1b** are shown below.

3-Hydroxy-2-(pyridin-2-yl)-4*H*-chromen-4-one (1a). The crude product (440 mg, 1.3 mmol) was recrystallized from EtOH to yield 380 mg (82%) of **1a**. ^{1}H NMR: δ 8.5 (m, 1H), 8.28 (m, 1H), 8.11 (d, *J* = 8 Hz, 1H), 7.96 (m, 1H), 7.64 (d, *J* = 1 Hz, 1H), 7.50 (d, *J* = 0.5 Hz, 1H), 7.48−7.41 (m, 1H), 7.39−7.33 (m, 1H). ^{13}C NMR: δ 173.6, 154.3, 152.5, 146.6,

which then channels into the proton transfer coordinate. Such a nuclear (hydrogen atom) motion coupled solvent polarization effect has been rationalized by a mechanism similar to the weak-coupling electron transfer described by the Marcus theory.[8c,9] Due to the relatively slow, solvent induced barrier coupled ESIPT rate, the associated dual emission and its ratiometric changes as a function of solvent polarity and/or electron donating/accepting strength have been exploited in several potential applications such as solvent polarity and metal ion sensors, etc.[10]

Herein, we report the synthesis, characterization and photophysical properties of a new class of functionalized 3HF derivatives. In this work, 3-hydroxy-2-(pyridin-2-yl)-4*H*-chromen-4-one (**1a**, see Scheme 1) was strategically designed such that the hydrogen bond could potentially be located at either OH---O=C or OH---N (pyridine) site, forming five- (**1a(O)**) and six-(**1a(N)**) membered ring HB configurations, respectively. For a comparative study, 3-hydroxy-2-(pyridin-4-yl)-4*H*-chromen-4-one (**1b**, Scheme 1) was also synthesized. Due to the lack of HB formation between the hydroxyl group and the pyridinic nitrogen, **1b** is expected to possess a unique five membered ring HB configuration between the hydroxyl group and carbonyl oxygen similar to that of 3HF. In this study, our aim mainly focuses on the spectroscopy and dynamics of the competitive intramolecular HB equilibrium between **1a(O)** and **1a(N)** and their associated ESIPT properties. The resulting different ESIPT

Intramolecular Proton Transfer Reaction

J. Phys. Chem. A, Vol. 113, No. 1, 2009 **207**

SCHEME 2: Relaxation Processes for Excited-State Charge Transfer Coupled Proton Transfer Demonstrated by *N,N*-Diethylamino-3-hydroxyflavones[8]
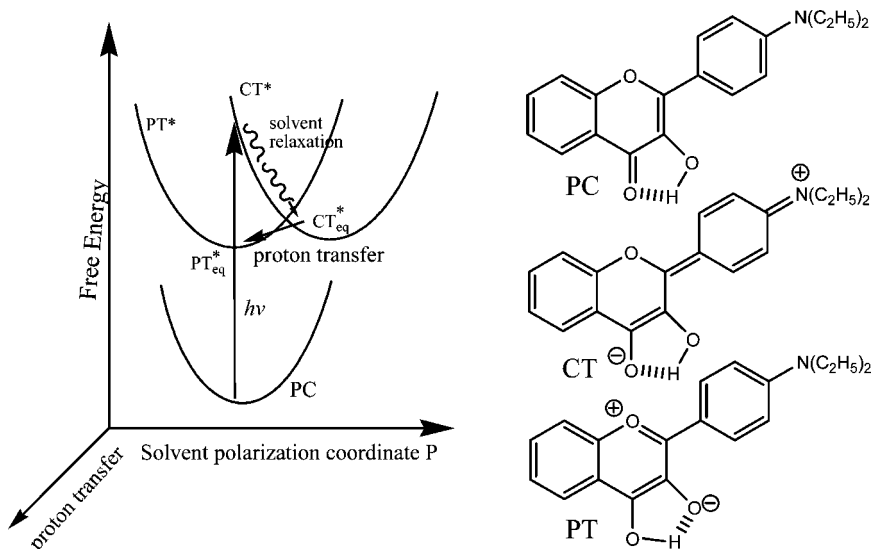
SCHEME 3: Synthetic Routes of 1a and 1b
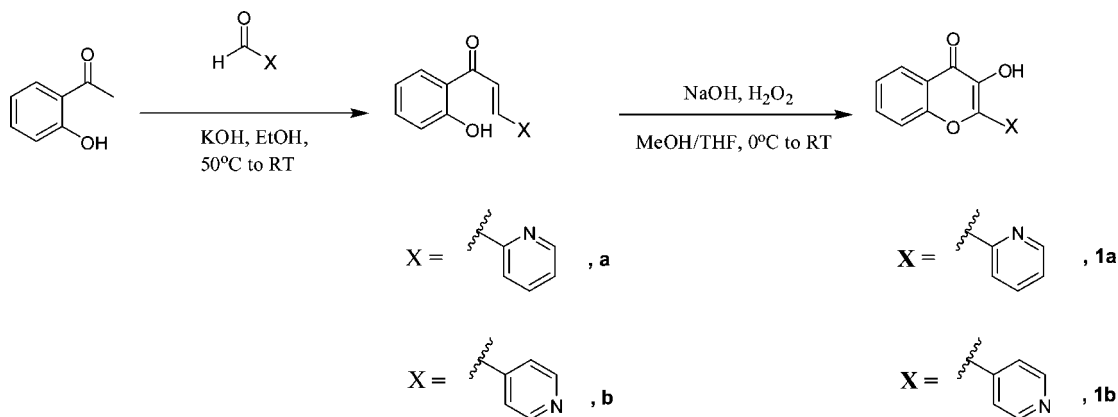
143.3, 139.5, 138.0, 133.3, 125.9, 124.0, 123.7, 122.9, 119.8, 117.6 FAB-MS: *m/z* 240.1 (M$^+$ + 1).

3-Hydroxy-2-(pyridin-4-yl)-4*H*-chromen-4-one (1b). The crude product (500 mg, 1.3 mmol) was recrystallized from EtOH to yield 400 mg (84%) of **1a**. ^{1}H NMR: δ 7.91−7.88 (m, 1H), 7.51−7.46 (m, 1H), 7.00−6.98 (m,1H), 6.93−6.91 (m, 1H), 6.89−6.83 (m, 2H), 6.79−6.75 (m, 2H). ^{13}C NMR: δ 173.7, 161.5, 143.3, 136.6, 130.7, 121.1, 119.5, 117.5, 115.5, 111.3, 107.94. FAB-MS: *m/z* 239.0 (M$^+$ + 1).

Crystallographic Data Collection and Refinement. Data collection of compound **1a(N)** was carried out on a NONIUS KappaCCD diffractometer with Mo radiation (λ = 0.71073 Å) at 150(1) K. A preliminary orientation matrix and unit cell parameters were determined from 15 frames, each frame corresponds to the 1degree ω scan in 20 s, followed by spot integration and least-squares refinement. Data were measured using ω scans, 0.50 degree per frame, 100 s. per degree. Cell parameters were retrieved and refined using *DENZO-SMN*[11] software on all observed reflections. Data reduction was performed with the *DENZO-SMN*[11] software. An empirical absorption was based on the symmetry-equivalent reflections and applied the data using the *SORTAV*.[12] program. The structure analysis was made by using *SHELXTL* program on PC computer. The structure was solved using the *SHELXS-97*[13] program and refined using *SHELXL-97*[14] program by full-matrix least-squares on F^2 values. All hydrogen atoms were generated

geometrically (C−H = 0.95) and refined using a riding mode with the exception of the hydrogen atom (H(2)) of hydroxyl group, which is located in the difference Fourier map with the corresponding positions. The final full-matrix, least-squares refinement on F^2 was applied for all observed reflections [I > 2σ(I)]. All calculations were performed using the SHELXTL software package.[15] Crystallographic data and details of data collections and structure refinements of **1a(N)** are listed in the Supporting Information.

Measurements. Steady-state absorption and emission spectra were recorded with a Hitachi (U-3310) spectrophotometer and an Edinburgh (FS920) fluorimeter, respectively. The various solvents were of spectragrade quality (Merck Inc.) and were used upon receipt. Benzene and acetonitrile showed traces of fluorescence impurities and were fractionally distilled prior to use. Nanosecond lifetime studies were performed with an Edinburgh FL 900 photon-counting system with a hydrogen-filled or a nitrogen lamp as the excitation source. The emission decays were analyzed by the sum of exponential functions, which allows partial removal of the instrument time broadening and thus renders a temporal resolution of ∼200 ps. The setup for picosecond dynamical measurements consisted of a femtosecond Ti-Sapphire oscillator (82 MHz, Spectra Physics). The fundamental train of pulses was pulse-selected (Neos, model N17389) to reduce the repetition rate to typically 0.8−8 MHz, and then used to produce second harmonics (375−425 nm) as
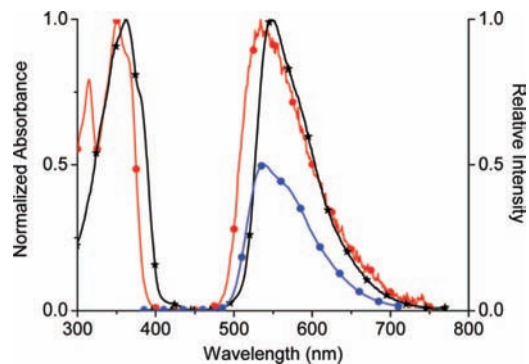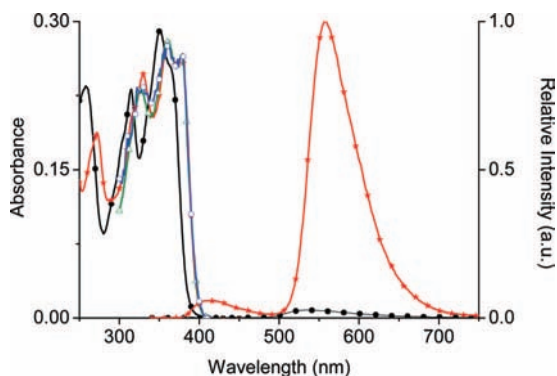
Figure 1. Normalized absorption and emission spectra of **1a** (red -●-) and **1b** (black -★-) in CH_2Cl_2 ($\sim 2 \times 10^{-5}$ M, $\lambda_{ex} \sim 350$ nm) and the single crystal emission of **1a** (blue -●-) ($\lambda_{ex} = 360$ nm).
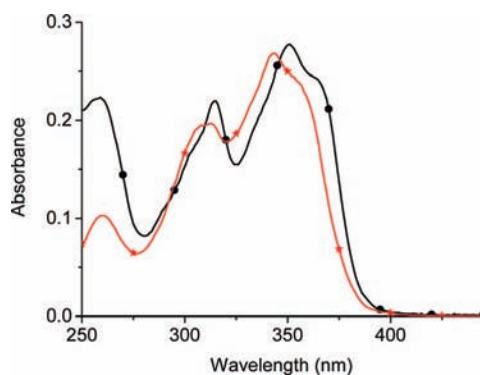

Figure 2. Absorption spectrum (black -●-) and the excitation spectrum (red -★-, monitored at 534 nm) of **1a** in CH_2Cl_2 ($\sim 2 \times 10^{-5}$ M).


Figure 3. Absorption and emission spectra of **1a** prior to the addition of $HCl_{(g)}$ (black -●-). The absorption and emission of **1a** ($\sim 2 \times 10^{-5}$ M) in CH_2Cl_2 purged with $HCl_{(g)}$ to reach the saturation (red -★-, see text for detail). The excitation spectra of **1a** in CH_2Cl_2 purged with $HCl_{(g)}$ to reach the saturation by monitoring at 430 nm (blue -○-) and 560 nm (green -△-), respectively.

an excitation light source. A polarizer was placed in the emission path to ensure that the polarization of the fluorescence was set at the magic angle (54.7°) with respect to that of the pump laser to eliminate fluorescence anisotropy. An Edinburgh OB 900-L time-correlated single photon counting system was used as a detecting system, rendering a temporal resolution of ∼15 ps.

Fluorescence upconversion measurements were performed with a femtosecond optically gated system (FOG-100, CDP). The fundamental of a Ti:sapphire laser (Spectra Physics) at 750−850 nm with an average power of 0.5 W and a repetition rate of 82 MHz was used to produce second harmonics (SH) at 375−425 nm by focusing onto a 0.5 mm thick BBO type-I crystal. The SH were then separated from the fundamental pulses with a dichroic mirror and used as the pump pulses. The pump
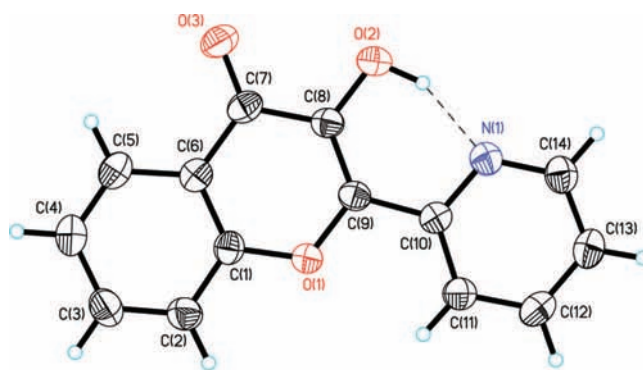

(a)
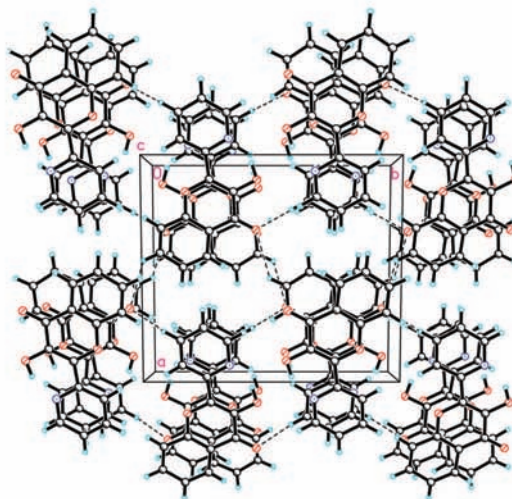
(b)
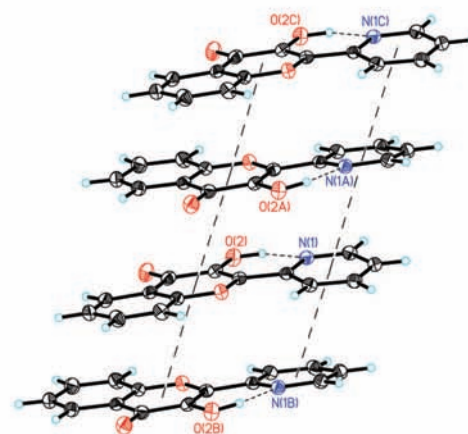
(c)

Figure 4. (a) The molecular structure of **1a** with thermal ellipsoids set at 50% probability level. (b) The molecular packing of **1a(N)** viewed along the *c*-axis. (c) The 1D chain-like architecture of **1a(N)** in an ABAB pattern (dashed line) through the $\pi-\pi$ intermolecular interaction among **1a(N)** molecules.

pulses were then focused onto a rotating cell, and the optical path length was 1.0 mm. The resulting fluorescence was collected by an achromatic lens and then focused on another BBO type-I crystal (0.5 mm). The optically delayed remaining fundamental pulses were also focused on the BBO crystal and used as gate pulses for the sum-frequency generation. A Berek's variable waveplate was placed in the pump beam path to ensure that the polarization of the pump laser was set at the magic angle (54.7°) with respect to that of the probe laser to eliminate

Intramolecular Proton Transfer Reaction

J. Phys. Chem. A, Vol. 113, No. 1, 2009 **209**
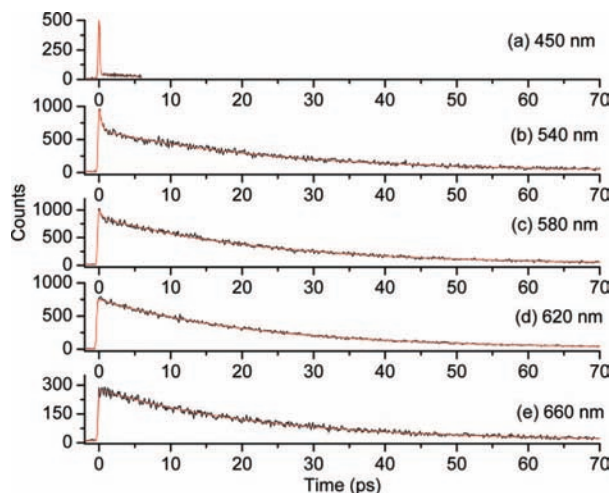
Figure 5. Time-resolved sum frequency signal of fluorescence at different wavelength and gate pulse (760 nm) for **1a** in CH_2Cl_2. The solid lines express the corresponding best-fitting curve.

fluorescence anisotropy. The upconverted signal was then separated by an F/4.9 (f = 380 mm) single monochromator (CDP2022) and detected via a photon counting PMT (R1527P, Hamamatsu). The cross correlation between SH and the fundamental had a full width at half-maximum (fwhm) of ~ 150 fs, which was chosen as a response function of the system.

An integrating sphere (Laboratory sphere) was applied to measure the quantum yield in the solid state, for which the solid thin film was prepared via direct vacuum deposition and excited by an argon ion laser at 363 nm. The resulting luminescence was acquired with an intensified charge-coupled detector for subsequent quantum yield analyses according to a reported method.[16]

Theoretical Approaches. The Gaussian 03 program was used to perform the ab initio calculation on the molecular structure.[17] Geometry optimizations for all structures were carried out with the 6-31G(d′) basis set to the B3LYP functional.[18,19] The hybrid DFT functional B3LYP has proven to be a suitable DFT functional to describe hydrogen bond.[20] Hessians and hence vibrational frequencies were also performed to check whether the optimized geometrical structures for those molecules were at energy minima, transition states, or higher order saddle points. After obtaining the converged geometries, the TD-B3LYP/6-31++G(d′,p′) was used to calculate the vertical excitation energies.[20,21]

3. Results and Discussion

3.1. Steady-State Approach. As depicted in Figure 1, **1a** (2×10^{-5} M) in CH_2Cl_2 exhibits an UV absorption spectrum with the lowest lying transition maximized at 351 nm. The absorption extinction coefficient of 1.7×10^4 M^{-1} cm^{-1} at 350 nm indicates that the $S_0 \rightarrow S_1$ is a $\pi\pi^*$ transition. Upon 350 nm excitation, as shown in Figure 1, an anomalously long wavelength emission band was resolved, with a peak wavelength at 534 nm. The large Stokes shift (9763 cm^{-1}) between absorption and emission peak frequencies is reminiscent of the occurrence of ESIPT in 3HF and its derivatives.[5,8] However, in sharp contrast to the identity indicated by absorption and fluorescence excitation spectra in 3HF, a significant difference between these two spectra was observed for **1a**, in which the lowest lying peak wavelength (343 nm) of the excitation spectrum is blue-shifted around 8 nm in comparison to that of the absorption (see Figure 2). Since the intensity of the excitation

wavelength had been calibrated, such a difference cannot be attributed to the difference in the wavelength-dependent response of the instrument between absorption and emission spectra. Furthermore, as ensured by various characterizations of its purity (see experimental section), the possibility of a spectral difference originating from traces of impurity is also discarded. Realizing that **1a** might exist in two HB isomers, i.e., **1a(O)** and **1a(N)** (see Scheme 1), in which **1a(N)** is subject to protonation due to the greater basicity in pyridinic nitrogen, we thus performed a simple test by purging HCl gas to **1a** in CH_2Cl_2. Such a titration procedure is supposed to protonate the pyridinic nitrogen and hence to block the formation of O−H---N HB. Figure 3 reveals the emission spectrum of **1a** in CH_2Cl_2 purged with $HCl_{(g)}$ to reach full protonation (until changes in the emission spectra cease). In comparison to neutral **1a**, the tautomer emission (560 nm) was increased by ~25 folds, accompanied by a rather small portion of the normal (430 nm) emission. It is worthy to point out here that the excitation spectrum monitored at both normal (430 nm) and tautomer emission (560 nm) of the protonated **1a** is exactly the same, which is also identical with respect to the absorption spectrum (see Figure 3), indicating that both 430 and 560 nm bands originate from the same ground-state species. Details of the associated relaxation dynamics for neutral versus protonated **1a** will be further discussed.

In light of the above observations, we thus conclude the existence of equilibrium between **1a(N)** and **1a(O)** HB conformers in CH_2Cl_2, in which the protonation blocks the **1a(N)** HB conformer, leading to the formation of **1a(O)H$^+$** HB conformer. Note that such **1a(O)** ⇌ **1a(N)** equilibrium in ground-state must be fast in terms of kinetics because ^{1}H NMR could not resolve any O−H peak. This viewpoint of equilibrium is also supported by the absorption and emission spectra of **1b**, in which only **1b(O)** HB conformer exists due to the lack of an O−H---N(pyridine) hydrogen bond. As a result, **1b** exhibits a unique tautomer emission maximized at 547 nm (see Figure 1), and the excitation spectrum (not shown here), which is independent of the monitored emission wavelength, is identical to the absorption profile. In brief, the results of steady-state UV absorption and fluorescence measurements imply an equilibrium between **1a(O)** and **1a(N)** in solution. The absorption profile for **1a(N)** is red-shifted with respect to that of **1a(O),** plausibly due to different degrees of hydrogen bond induced π electron delocalization (vide infra). Upon excitation, **1a(O)** undergoes fast ESIPT, giving rise to a unique 534 nm tautomer emission. In sharp contrast, no steady-state emission could be resolved for **1a(N)** in CH_2Cl_2 as well as in other polar, aprotic solvents such as toluene and acetonitrile. Further insight into the relaxation dynamics of **1a(N)** will be elaborated in the section of fluorescence up-conversion measurement.

Single crystals of **1a** were also successfully grown. As shown in Figure 4a, the X-ray structural determination reveals a dominant **1a(N)** population in a single crystal form, which exhibits a intramolecular O(2)---N(1) hydrogen bond with N---O distance of 2.589(2) Å. The small dihedral angle (4.36°) of N(1)−C(10)−C(9)−C(8) reveals that the 2-pyridyl moiety is nearly coplanar with respect to the parent chromone moiety. This result can be rational by the O(2)---N(1) hydrogen bond formation together with partial π bond character of C(9)−C(10) with bond distance of 1.462(2) Å. It is important to note that adjacent **1a(N)** molecules are parallel and superimposed in an ABAB pattern (Figure 4b) to form a 1D chain-like architecture (Figure 4c) through the $\pi-\pi$ intermolecular interactions between the pyridyl−pyridyl moieties and between chromone−chromone

TABLE 1: Photophysical Properties of 1a, 1a(O)H$^+$ in CH$_2$Cl$_2$, and 1a in Single Crystal^a

	λ_{abs}/nm	λ_{em}/nm	relaxation dynamics/ps^b
		1a	
CH$_2$Cl$_2$	351	N: –	450 nm [τ_1= 0.13 (0.98), τ_2= 28.9 (0.02)]
		T: 534	540 nm [τ_1= 0.35 (0.37), τ_2= 22.8 (0.63)]
			580 nm [τ_1= 0.24 (0.18), τ_2= 22.6 (0.82)]
			620 nm [τ_1= 0.42 (0.03), τ_2= 22.6 (0.97)]
			660 nm [τ= 22.4]
			660 nm [τ_1= 24(0.96), τ_2= 1400 (0.04)]^c
single crystal		N: –	
		T: 540	540 nm [τ= 3500]^c
77 K CH$_2$Cl$_2$		T: 528	530 nm [τ= 4900]^c
		1a(O)H$^+$	
CH$_2$Cl$_2$	361	N: 430	430 nm [τ= 15.7]
		T: 560	580 nm [τ_1= 14.8 (−0.48), τ_2= 647 (0.52)]

^{a} The experimental error for the fitted time constant is less than ∼10%. ^{b} Data in parentheses are the fitted pre-exponential factor. ^{c} The relaxation dynamics were measured by time-correlated single photon counting.
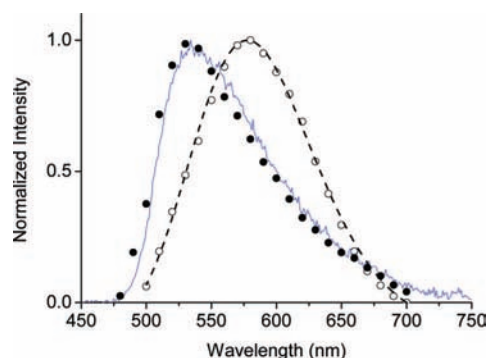
Figure 6. (Blue-solid line) Steady state emission spectrum. (●) Spectrum taken by plotting the pre-exponential value of the 1.4 ns decay component versus the monitored wavelength. (○) Spectrum taken by plotting the pre-exponential value of the 22.6 ps decay component versus the monitored wavelength for **1a** in CH$_2$Cl$_2$. (Dashed line) The best-fitted spectrum of the 22.6 ps (○) component.
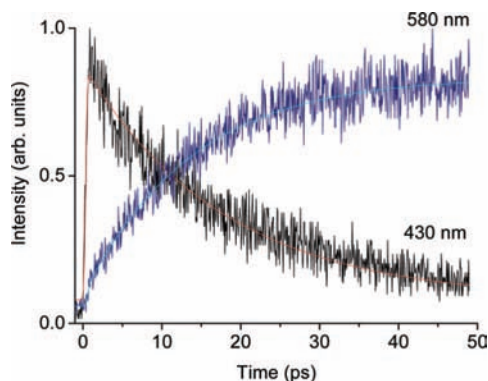
Figure 7. Time-resolved sum frequency signal of fluorescence and gate pulse (780 nm) for **1a** in CH$_2$Cl$_2$. The solid lines express the corresponding best-fitting curve. The black solid line denotes the decay monitored at the emission of 430 nm and the blue solid line represents the rise and decay of the 580 nm emission.

moieties, respectively, with the distances of 3.713 and 3.709 Å between the ring centroids. These results are essentially in agreement with the previous report about the crystal molecular structure of 2-(1*H*-benzimidazol-2-yl)-3-hydroxy-4*H*- chromen-4-one.[22]

3.2. ESIPT Dynamics. More insight into the mechanism of ESIPT for **1a** may be resolved by the associated relaxation dynamics. Figures 5a–e show the time-resolved up-converted fluorescence signal of **1a** (1 × 10^{-3} M in CH$_2$Cl$_2$) at various emission wavelengths (λ_{ex} ∼ 380 nm). Pertinent spectroscopic

and dynamic data are listed in Table 1. Upon monitoring at 450 nm, which is supposed to be in the normal emission region but could not be resolved from a steady state manner due to fast ESIPT (vide supra), the time-resolved 450 nm emission is composed of response limited rise and decay (<150 fs) components (see Figure 5a). On the other hand, when monitoring exclusively at the tautomer emission region of e.g. 660 nm, as shown in Figure 5e, multiexponential decay curves were observed. The best deconvoluted fitting of the relaxation dynamics renders a response limit risetime (<150 fs), a fast but resolvable decay, and a nearly constant value (within the acquisition time of 100 ps) with a small pre-exponential factor contribution (<4%) compared with the fast decay (∼96%) components. The system response limited decay for the normal emission as well as rise for the tautomer emission unambiguously indicates an ultrafast rate of ESIPT. The fast and resolvable decay time constant was measured to be 22.6 ± 0.3 ps. The very long decay constant indeed is attributed to a long population decay, which was further resolved to be 1.4 ns by the time-correlated single photon counting measurement.

We then took the fitted pre-exponential value of the 22.6 ps decay component at various monitored wavelengths and plotted the emission intensity versus wavelength, shown in Figure 6. Obviously, the up-converted emission of the fast decay (22.6 ps) component was maximized at ∼577 nm, which is significantly red-shifted with respect to the 534 nm peak obtained with the steady state measurement. On the other hand, upon integrating the long-decay (1.4 ns) component, the plot for the emission intensity versus emission wavelength reveals a maximum at ∼530 nm (see Figure 6), which is consistent with that obtained from the steady state measurement. Thus, the relaxation dynamics, in combination with the steady state results, show that both conformers **1a(O)** and **1a(N)** undergo ESIPT reaction in solution (e.g., CH$_2$Cl$_2$). Following ESIPT, **1a(O)** gives rise to a tautomer emission maximized at 534 nm with an observed lifetime of 1.4 ns in CH$_2$Cl$_2$, while the tautomer emission for **1a(N)** undergoes a fast decay constant of 22.6 ps and its intensity is too weak to be resolved in a steady state manner. Note that the normal emission of **1a(N)**, although it could not be resolved with a steady state means, is expected to be red-shifted compared to that of **1a(O)**. This viewpoint is supported by the time-resolved fluorescence monitored at shorter wavelengths such as 540 nm (see Figure 5b), in which in addition to the 22.6 ps decay component, the time-resolved profile also exhibits an ultrafast, unresolvable decay component (<150 fs). Finally, ultrafast ESIPT also takes place for **1a(N)** in the crystal, as

Intramolecular Proton Transfer Reaction

J. Phys. Chem. A, Vol. 113, No. 1, 2009 **211**
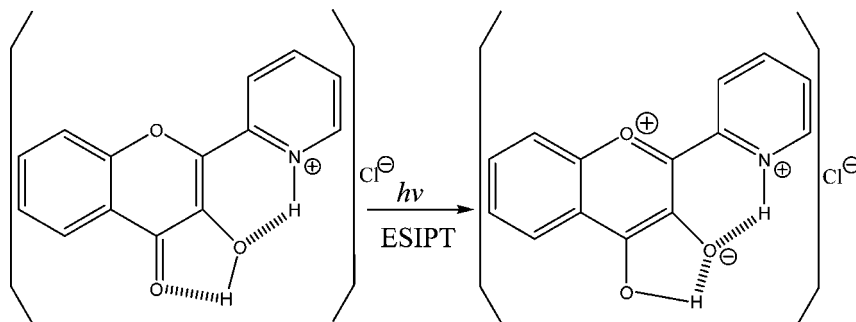
Figure 8. Proposed ESIPT mechanism of **1a(O)H$^+$**. Note that a large change of the dipole moment is expected during the ESIPT process (see text for detailed discussion).

SCHEME 4: Calculated Energy Potential Diagram of 1a with Dual ESIPT Pathways after Applying Solvation in CH$_2$Cl$_2$[a]
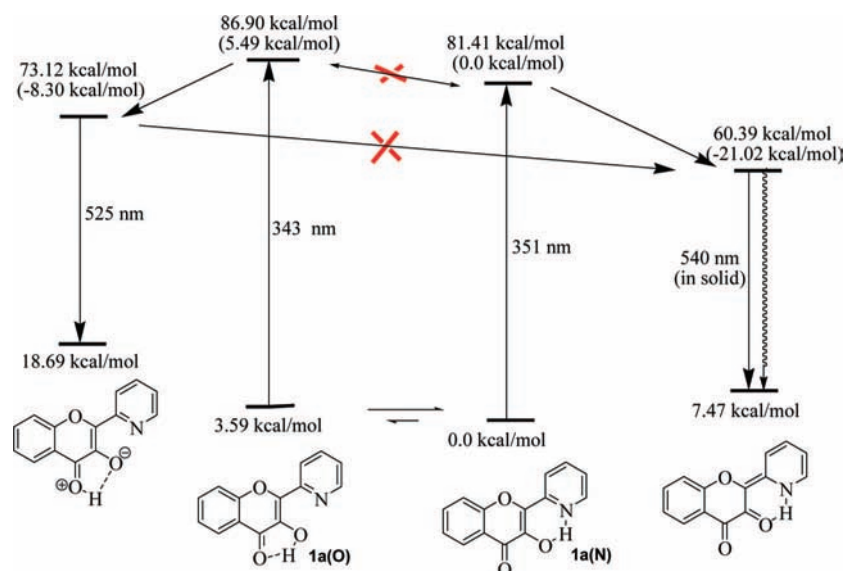
[a] The absorption and emission gaps were taken from the experimental data. See detailed discussion in the text.
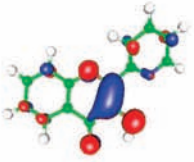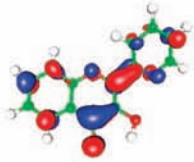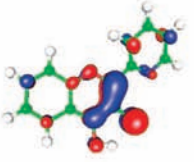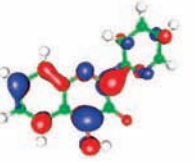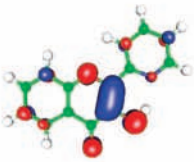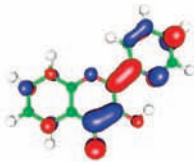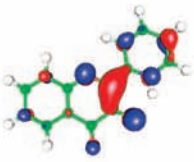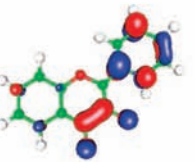
supported by the large Stokes shifted fluorescence with a system response risetime (<150 fs), while the prohibition of the nonradiative decay process (vide infra) in the single crystal leads to a bright 540-nm tautomer emission ($\Phi_f \sim 0.3$) with a lifetime as long as 3.5 ns.

One intriguing feature lies in the relaxation dynamics of the protonated form, i.e., **1a(O)H$^+$** in CH$_2$Cl$_2$. Dual emission ascribed to normal (430 nm) and tautomer (560 nm) species was resolved for **1a(O)H$^+$** in CH$_2$Cl$_2$ (see Figure 3, vide supra). Upon monitoring at the normal emission of 430 nm, the time-resolved signal is composed of a response-limited rise (<150 fs) and a single exponential decay of 15.7 ps (see Figure 7). On the other hand, the relaxation dynamics monitored at the tautomer emission of 560 nm are established by a resolvable rise (14.8 ps) and a rather long decay component (647 ps). Note that the latter data are acquired by the time-correlated single photon counting technique. Within experimental and fitting uncertainty, the decay of the normal emission is matched with respect to the ris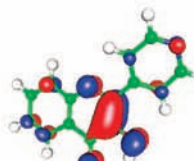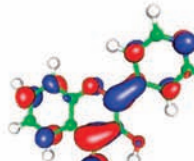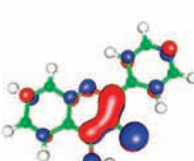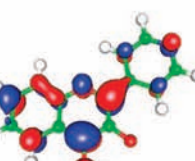e of tautomer emission, consistent with a precursor–successor type of ESIPT relationship. Although the dynamics are clearly resolved, in comparison to the > (150 fs)$^{-1}$ rate of ESIPT in **1a(O)** (or **1a(N)**) in neutral form, the much slower ESIPT time scale (~15 ps) in **1a(O)H$^+$** is intriguing. On one hand, it may imply the rise of an intrinsic, appreciable barrier during ESIPT for **1a(O)H$^+$**. However, since the driving force of the forming oxy-anion dual hydrogen bonds (see Figure 8) is greater than that of the single hydrogen bond in **1a(O)**,

this hypothesis, in our view, may be groundless. Alternatively, it is more plausible that the cationic form **1a(O)H$^+$** and its proton transfer tautomer possess drastically different dipole moments in the excited state, such that the solvent polarity induced barrier is appreciable, which then channels into the ESIPT reaction.[8] Nevertheless, this viewpoint requires more rigorous examination, including solvent polarity dependent studies with both steady-state and dynamics approaches, which is not the main focus of this study. Details will be addressed in future work.

We have also made attempts to extract the associated thermodynamic parameters of the HB equilibrium via a temperature-dependent absorption study. Unfortunately, owing to the relatively high freezing point (223 K) of CH$_2$Cl$_2$ and great similarities in spectral profiles between **1a(O)** and **1a(N)**, we failed to obtain the thermodynamics via the steady state approach. Alternatively, we realize that the ratios of the pre-exponential factors for 22.6 ps versus 1.4 ns component are within 22 to 32 in the monitored emission range of 540−580 nm. Assuming that **1a(O)** and **1a(N)** exhibit very similar radiative lifetime, i.e., the same transition dipole due to the similarities in spectral features (in terms of spectral profile and absorptivity), we qualitatively estimate the ground-state equilibrium constant for **1a(O)**⇌**1a (N)** in 298 K CH$_2$Cl$_2$ to be within 27 ± 5 M^{-1}. The thermally favorable **1a(N)** population can be rationalized by the greater basicity of pyridinic nitrogen

TABLE 2: Theoretical Results on Energy and Frontier Orbitals of Various Electronic States of 1a(O), 1a(N), and 1b

1a(O) (normal form)					1a(O) (tautomeric form)			
state	Excitation	E_{cal} (eV)	λ_{cal} (nm)	(f)	Excitation	E_{cal} (eV)	λ_{cal} (nm)	(f)
S_1	HOMO→LUMO(+83%)	3.74	331.8	0.2587	HOMO→LUMO(+72%)	2.59	478.4	0.2709
S_2	HOMO-2→LUMO(+51%), HOMO-3→LUMO(30%), HOMO-1→LUMO(10%)	4.03	308.8	0.0027	HOMO-1→LUMO(+94%)	2.88	430.8	0.0129
	HOMO		LUMO		HOMO		LUMO	

1a(N) (normal form)					1a(N) (tautomeric form)			
state	Excitation	E_{cal} (eV)	λ_{cal} (nm)	(f)	Excitation	E_{cal} (eV)	λ_{cal} (nm)	(f)
S_1	HOMO→LUMO(+81%)	3.63	341.7	0.2379	HOMO→LUMO(+60%), HOMO→LUMO+1(23%)	2.81	441.5	0.1422
S_2	HOMO→LUMO+1(+92%)	4.05	306.4	0.0163	HOMO→LUMO+1(+68%), HOMO→LUMO(+16%)	3.15	393.6	0.1943
	HOMO		LUMO		HOMO		LUMO	

1b (normal form)					1b (tautomeric form)			
state	excitation	E_{cal} (eV)	λ_{cal} (nm)	(f)	Excitation	E_{cal} (eV)	λ_{cal} (nm)	(f)
S_1	HOMO→LUMO(+82%)	3.79	327.1	0.2538	HOMO→LUMO(+73%)	2.67	463.8	0.2538
S_2	HOMO-1→LUMO(+73%) HOMO-4→LUMO(17%)	3.98	311.7	0.0011	HOMO-1→LUMO(+85%), HOMO-3→LUMO(12%)	3.09	401.5	0.0011
	HOMO		LUMO		HOMO		LUMO	

(c.f. carbonyl oxygen), together with the associated six membered ring HB geometry (c.f. five membered-ring HB structure in **1a(O)**).

3.3. Theoretical Approach. Supplementary support of the ground-state thermodynamics is provided by the computational approach (see Experimental Section). The full geometry optimization based on the B3LYP/6-31G(d′) theoretical level reveals that **1a(N)** is more stable than **1a(O)** by 3.79 kcal/mol in gas phase. It is worthy to note that if considering the polarization function on hydrogen such as 6-31G(d′,p′), the optimized geometry of the tautomeric form of **1a(O)** is converged to **1a(O)**. The result implies that the tautomer form of **1a(O)** in the ground-state is very unstable with respect to the normal forms, such that the **1a(O)** proton transfer tautomer ⇀ **1a(O)** reverse proton transfer may be rather small or even barrierless. After applying solvation in CH₂Cl₂ based on Onsager theory, the difference in energy is reduced to 3.59 kcal/mol, still in favor of **1a(N)**, qualitatively in agreement with that estimated experimentally. Further calculations show that the corresponding proton-transfer tautomer is higher in energy than the respective **1a(O)** and **1a(N)** by 15.10 and 7.47 kcal/mol in the ground state. To each ground-

state we then simply add absorption and emission peak frequency (see Figures 1) to mark the energy level of the corresponding S_1 state. As a result, the overall energetics is depicted in Scheme 4. The results clearly indicate that ESIPT for both **1a(O)** and **1a(N)** is thermodynamically favorable, consistent with the experimental results.

Another interesting feature lies in the frontier orbital analysis. On the basis of time dependent DFT (TD-DFT), the $S_0 \rightarrow S_1$ $\pi\pi^*$ transition was calculated to be 3.49 eV (355 nm) and 3.43 eV (361 nm) for **1a(O)** and **1a(N)**, respectively, the results of which are well-correlated with the peak (343 nm) of excitation spectrum for **1a(O)** and an expected red-shifted absorption of **1a(N)**. The frontier orbital analyses reveal that the π-electron density of the proton-transfer tautomer form of **1a(O)** in the excited-state is mainly delocalized at the chromone moiety, while that of the tautomer form of **1a(N)**, in sharp contrast, is largely spread around the pyridine moiety and extended to the carbonyl oxygen. As expected, the former is similar to the electronic configuration of **1b** tautomer (see Table 2). The results manifest two different electronic configurations of tautomers resulting from ESIPT of two respective isomers. Due to the

drastically different lifetimes measured in this study (vide supra), the interconversion between these two proton-transfer tautomers in the excited-state is not likely to occur. This can be rationalized by the necessity of breaking the strong hydrogen bond for interconversion, the time scale of which seems to be incomparable with the respective relaxation dynamics. Likewise, the conversion between excited **1a(O)** and **1a(N)** species is also prohibited due to the ultrafast rate of ESIPT for each isomer in the excited state (see Scheme 4).

3.4. Relaxation after ESIPT. Last but not least, after ESIPT, the dominant radiationless deactivation process for **1a(N)** tautomer in solution is also of fundamental interest. As supported by the above X-ray analysis, the associated photophysics of **1a** in a single crystal clearly originate from the **1a(N)** conformer. As depicted in Figure 1, independent of the excitation wavelength, the **1a(N)** conformer in solid exhibit a unique, bright emission maximized at 540 nm. In comparison to the onset of the absorption spectrum of ∼400 nm, the large Stokes shifted emission warrants the occurrence of ESIPT in **1a(N)** solid crystal, resulting in the 540 nm tautomer emission. This is in sharp contrast to the lack of steady-state emission for **1a(N)** in CH_2Cl_2 and other solvents. The results are reminiscent of many ESIPT molecules exhibiting extremely weak tautomer emission in solution due to cis−trans isomerization, which induces a dominant deactivation channel for the emission quenching in the excited state.[4] For example, in the case of 2-(2′-hydroxyphenyl)benzothiazole, it has been well-known that following ESIPT, cis-tran isomerization takes place in the excited state.[23] In the case of **1a(N)** in solution, once forming the keto-tautomer via ESIPT (see Scheme 1), it seems that the cis−trans isomerization along C(9)−C(10) rotation may play a key role to account for the dominant radiationless deactivation process. As for an extreme case, crossover of the ground and excited-state potential energy surface alone rotational coordinate may lead to the formation of conical intersections.[24] It is thus plausible that radiationless decay of **1a(N)** proton-transfer tautomer would be associated with the seam of conical intersection with a sloped topology lying parallel to the C(9)−C(10) rotational pathway.

Alternatively, it is also possible that the tautomer is subject to a dynamical quenching effect, induced via an excited-state charge transfer complex between solute and solvent, as has been demonstrated that was acting for a dual intramolecular hydrogen bonded 3-hydroxyflavone derivative, 2,8-diphenyl-3,7,-dihydroxy-4*H*,6*H*-pyrane[3,2-*g*]chromene-4,6dione, a diflavonol molecule which has the possibility of single-proton transfer of double-proton transfer.[25] To examine this, luminescence of **1a** in 77 K CH_2Cl_2 solid matrix was performed and the photophysical data are listed in Table 1. Due to the thermally favorable **1a(N)** (vide infra), one expected **1a(N)** to be the dominant species at 77 K. Evidently, in 77 K CH_2Cl_2, solid matrix, a bright **1a(N)** tautomer emission maximized at 528 nm was resolved (Φ_f ∼0.41, τ_f = 4.9 ns, see Table 1). Since both solvent diffusion and cis−trans rotation are prohibited in 77 K CH_2Cl_2 solid matrix, the results cannot single out the associated quenching mechanism. At current stage, however, the observation of highly emissive **1a(N)** tautomer emission in a single crystal leads us to be favorable on the deactivation pathway incorporating cis−trans isomerism.

4. Conclusion

In conclusion **1a** has been synthesized and characterized and its dual ESIPT channels explored. In the solid state, **1a** exists exclusively in **1a(N)** HB conformer, which, upon excitation, undergoes ESIPT from the hydroxyl proton to the pyridinic nitrogen, forming a keto-tautomer emitting at 540 nm. In solution such as CH_2Cl_2, **1a** exists in two HB isomers **1a(O)** and **1a(N)** with an equilibrium constant of ∼22−32 in favor of **1a(N).** Both isomers undergo ultrafast (<150 fs) ESIPT, forming a zwitterion and keto-tautomer, respectively, in the excited state. A fast radiationless pathway, possibly induced by the C(9)−C(10) rotational deactivation, then takes place in the keto-tautomer, resulting in the lack of steady-state emission. To our best knowledge, this is the first time that such a dual channel ESIPT pathway with comprehensive reaction dynamics is investigated in the case of 3-HF relevant ESIPT molecules. As shown in the proton titration, the resulting on (with H^+)/off (without H^+) emission property for the **1a(O)** versus **1a(N)** tautomer fluorescence may lead to future studies in e.g. reversible Lewis acid/basis detection in organic solvents.

References and Notes

(1) For instance: *Studies in physical and theoretical Chemistry*; Müller, A., Ratajack, H., Junge, W., Diemann, E., Eds.; Electron and Proton Transfer in Chemistry and Biology 78; Elsevier: Amsterdam, 1992.

(2) (a) Scheiner, S. *J. Phys. Chem. A* **2000**, *104*, 5898. (b) Waluk, J. Conformational Aspects of Intra- and Intermolecular Excited-State Proton Transfer In *Conformational Analysis of Molecules in Excited States*; Waluk, J., Ed.; Wiley-VCH: New York, 2000. (c) Chou, P. T. *J. Chin. Chem. Soc.* **2001**, *48*, 651. (d) Wu, K. C.; Cheng, Y. M.; Lin, Y. S.; Yeh, Y. S.; Pu, S. C.; Hu, Y. H.; Yu, J. K.; Chou, P. T. *Chem. Phys. Lett.* **2004**, *382*, 203. (e) Paterson, M. J.; Robb, M. A.; Blancafort, L.; DeBellis, A. D. *J. Am. Chem. Soc.* **2004**, *126*, 2912. (f) Lochbrunner, S.; Wurzer, A. J.; Riedle, E. *J. Phys. Chem. A* **2003**, *107*, 10580. (g) de Vivie-Riedle, R.; De Waele, V.; Kurtz, L.; Riedle, E. *J. Phys. Chem. A* **2003**, *107*, 10591. (h) Cheng, C. C.; Chang, C. P.; Yu, W. S.; Hung, F. T.; Liu, Y. I.; Wu, G. R.; Chou, P. T. *J. Phys. Chem. A* **2003**, *107*, 1459. (i) Lukeman, M.; Wan, P. *J. Am. Chem. Soc.* **2003**, *125*, 1164.

(3) For example, see: (a) Chou, P. T.; McMorrow, D.; Aartsma, T. J.; Kasha, M. *J. Phys. Chem.* **1984**, *88*, 4596. (b) Ernsting, N. P.; Nikolaus, B. *Appl. Phys. B: Laser Opt.* **1986**, *39*, 155. (c) Acuña, A. V.; Amat-Guerri, F.; Cataln̄, J.; Costella, A.; Figuera, J.; Munoz, *J. Chem. Phys. Lett.* **1986**, *132*, 576. (d) Kasha, M. In *Molecular Electronic Devices*; Carter, F. L., Siatkowski, R. E., Wohltjen, H., Eds.; Elsevier Science Publishers: New York, 1988; pp 107−121. (e) Cataln̄, J.; del Valle, J. C. *J. Am. Chem. Soc.* **1993**, *115*, 4321. (f) Ferrer, M. L.; Acuña, A. U.; Amat-Guerri, F.; Costela, A.; Figuera, J. M.; Florido, F.; Sastre, R. *Appl. Opt.* **1994**, *33*, 2266. (g) Jones, G.; Rahman, M. A. *J. Phys. Chem.* **1994**, *98*, 13028. (h) Liphardt, M.; Gooneskera, A.; Jones, B. E.; Ducharme, S.; Takacs, J. M.; Zhang, L. *Science (Washington, D.C.)* **1994**, *263*, 367. (i) Kuldová, K.; Corval, A.; Trommsdorff, H. P.; Lehn, J. M. *J. Phys. Chem. A* **1997**, *101*, 6850. (j) Sytnik, A.; Gormin, D.; Kasha, M. *Proc. Natl. Acad. Sci. U.S.A.* **1994**, *91*, 8267. 11968. (k) Sytnik, A.; del Valle, J. C. *J. Phys. Chem.* **1995**, *99*, 13028. (l) Roshal, A. D.; Grigorovich, A. V.; Doroshenko, A. O.; Pivovarenko, V. G.; Demchenko, A. P. *J. Phys. Chem. A* **1998**, *102*, 5907. (m) Tarkka, R. M.; Zhang, X.; Jenekhe, S. A. *J. Am. Chem. Soc.* **1996**, *118*, 9438.

(4) Chen, K. Y.; Cheng, Y. M.; Lai, C.-H.; Hsu, C. C.; Ho, M. L.; Lee, G. H.; Chou, P. T. *J. Am. Chem. Soc.* **2007**, *129*, 4534.

(5) (a) Sengupta, P. K.; Kasha, M. *Chem. Phys. Lett.* **1979**, *68*, 382.

(6) (a) McMorrow, D.; Kasha, M. *J. Phys. Chem.* **1984**, *88*, 2235. (b) Chou, P.; McMorrow, D.; Aartsma, T. J.; Kasha, M. *J. Phys. Chem.* **1984**, *88*, 4596. (c) Kasha, M. *J. Chem. Soc., Faraday Trans. 2* **1986**, *82*, 2379. (d) Etter, M. C.; Urbańczyk-Lipkowska, Z.; Baer, S.; Barbara, P. F. *J. Mol. Struct.* **1986**, *144*, 155. (e) Brucker, G. A.; Kelley, D. F. *J. Phys. Chem.* **1988**, *92*, 3805. (f) Schwartz, B. J.; Peteanu, L. A.; Harris, C. B. *J. Phys. Chem.* **1992**, *96*, 3591. (g) Ameer-Beg, S.; Ormson, S. M.; Brown, R. G; Matousek, P.; Towrie, M.; Nibbering, E. T. J.; Foggi, P.; Neuwahl, F. V. R. *J. Phys. Chem. A* **2001**, *105*, 3709. (h) Bader, A. N.; Ariese, F.; Gooijer, C. *J. Phys. Chem. A* **2002**, *106*, 2844. (i) Bader, A. N.; Picocarenko, V. G.; Demchenko, A. P.; Ariese, F.; Gooijer, C. *J. Phys. Chem. B* **2004**, *108*, 10589.

(7) Chudoba, C.; Riedle, E.; Pfeiffer, M.; Elsaesser, T. *Chem. Phys. Lett.* **1996**, *263*, 622.

(8) (a) Chou, P. T.; Martinez, M. L.; Clements, J. H. *J. Phys. Chem.* **1993**, *97*, 2618. (b) Chou, P. T.; Martinez, M. L.; Clements, J. H. *Chem. Phys. Lett.* **1993**, *204*, 395. (c) Swinney, T. C.; Kelley, D. F. *J. Chem. Phys.* **1993**, *99*, 211. (d) Parsapour, F.; Kelley, D. F. *J. Phys. Chem.* **1996**, *100*, 2791. (e) Ormson, S. M.; Brown, R. G.; Vollmer, F.; Rettig, W. *J. Photochem. Photobiol. A* **1994**, *81*, 65. (f) Chou, P. T.; Huang, C. H.; Pu, S. C.; Cheng, Y. M.; Liu, Y. H.; Wang, Y.; Chen, C. T. *J. Phys. Chem. A.* **2004**, *108*, 6452. (g) Cheng, Y. M.; Pu, S. C.; Yu, Y. C.; Chou, P. T.; Huang, C. H.; Chen, C. T.; Li, T. H.; Hu, W. P. *J. Phys. Chem. A* **2005**, *109*, 3777.

(9) (a) Marcus, R. A. *J. Chem. Phys.* **1965**, *43*, 379. (b) Marcus, R. A. *Annu. Rev. Phys. Chem.* **1964**, *15*, 155. (c) Marcus, R. A. *J. Chem. Phys.* **1965**, *43*, 679. (d) Marcus, R. A. *Rev. Mod. Phys.* **1993**, *65*, 599.

(10) (a) Bublitz, G. U.; Boxer, S. G. *Annu. Rev. Phys. Chem.* **1997**, *48*, 213. (b) Klymchenko, A. S.; Demchenko, A. P. *J. Am. Chem. Soc.* **2002**, *124*, 12372. (c) Klymchenko, A. S.; Demchenko, A. P. *Phys. Chem. Chem. Phys.* **2003**, *5*, 461.

(11) DENZO-SMN, Otwinowski & Minor, 1997.

(12) SORTAV Blessing, R. H. *Acta Crystallogr., Sect. A* **1995**, *A51*, 33–38.

(13) SHELXS-97 Sheldrick, G. M. *Acta Crystallogr., Sect. A* **1990**, *A46*, 467–473.

(14) Sheldrick, G. M. *SHELXL-97*; University of Göttingen: Göttingen, Germany, 1997.

(15) *SHELXTL: Structure analysis program, version 6.10*; Bruker-axs: Madison, WI, 2000.

(16) de Mello, J. C.; Wittmann, H. F.; Friend, R. H. *Adv. Mater.* **1997**, *9*, 230.

(17) *Gaussian 03, Revision C.02* Frisch, M. J. ; Trucks, G. W.; Schlegel, H. B.; Scuseria, G. E.; Robb, M. A.; Cheeseman, J. R.; Montgomery, J. A., Jr.; Vreven, T.; Kudin, K. N.; Burant, J. C.; Millam, J. M.; Iyengar, S. S.; Tomasi, J.; Barone, V.; Mennucci, B.; Cossi, M.; Scalmani, G.; Rega, N.; Petersson, G. A.; Nakatsuji, H.; Hada, M.; Ehara, M.; Toyota, K.; Fukuda, R.; Hasegawa, J.; Ishida, M.; Nakajima, T.; Honda, Y.; Kitao, O.; Nakai, H.; Klene, M.; Li, X.; Knox, J. E.; Hratchian, H. P.; Cross, J. B.; Adamo, C.; Jaramillo, J.; Gomperts, R.; Stratmann, R. E.; Yazyev, O.; Austin, A. J.; Cammi, R.; Pomelli, C.; Ochterski, J. W.; Ayala, P. Y.; Morokuma, K.; Voth, G. A.; Salvador, P.; Dannenberg, J. J.; Zakrzewski, V. G.; Dapprich, S.; Daniels, A. D.; Strain, M. C.; Farkas, O.; Malick, D. K.; Rabuck, A. D.; Raghavachari, K.; Foresman, J. B.; Ortiz, J. V.; Cui, Q.; Baboul, A. G.; Clifford, S.; Cioslowski, J.; Stefanov, B. B.; Liu, G.; Liashenko, A.; Piskorz, P.; Komaromi, I.; Martin, R. L.; Fox, D. J.; Keith, T.; Al-Laham, M. A.; Peng, C. Y.; Nanayakkara, A.; Challacombe, M.; Gill, P. M. W.; Johnson, B.; Chen, W.; Wong, M. W.; Gonzalez, C.; Pople, J. A. Gaussian, Inc.: Wallingford, CT, 2004.

(18) Petersson, G. A.; Al-Laham, M. A. *J. Chem. Phys.* **1991**, *94*, 6081.

(19) (a) Becke, A. D. *Phys. Rev. A* **1988**, *38*, 3098. (b) Lee, C.; Yang, W.; Parr, R. G. *Phys. Rev. B* **1988**, *37*, 785.

(20) Koné, M.; Illien, B.; Graton, J.; Laurence, C. *J. Phys. Chem. A* **2005**, *109*, 11907.

(21) Stratmann, R. E.; Scuseria, G. E.; Frisch, M. J. *J. Chem. Phys.* **1998**, *109*, 8218.

(22) Svechkarev, D. A; Baumer, V. N.; Syzova, Z. A.; Doroshenko, A. O. *J. Mol. Struct.* **2008**, *882*, 63.

(23) (a) Brewer, W. E.; Martinez, M. L.; Chou, P. T. *J. Phys. Chem.* **1990**, *94*, 1915. (b) Ikegami, M.; Arai, T. *J. Chem. Soc., Perkin Trans.* **2002**, *2*, 1296.

(24) Weber, W.; Helms, V.; McCammon, J. A.; Langhoff, P. W. *Pro. Natl. Acad. Sci. U.S.A.* **1999**, *96*, 6177.

(25) (a) Falkovskaia, E.; Pivovarenko, V. G.; del Valle, J. C. *Chem. Phys. Lett.* **2002**, *352*, 415. (b) Falkovskaia, E.; Pivovarenko, V. G.; del Valle, J. C. *J. Phys. Chem. A* **2003**, *107*, 3316.